IEEE Access
Multidisciplinary ⋮ Rapid Review ⋮ Open Access Journal

Received 12 January 2024, accepted 4 February 2024, date of publication 21 February 2024, date of current version 29 February 2024.

Digital Object Identifier 10.1109/ACCESS.2024.3368694

APPLIED RESEARCH

Robust Isotropic Residual-Constrained VMD: A Novel Filter for Analyzing Engineering Surface Topography

QIN WEN AND NIANQING TANG
School of Artificial Intelligence, Neijiang Normal University, Neijiang, Sichuan 641100, China
Corresponding author: Nianqing Tang (17982950@qq.com)

This work was supported in part by the Scientific Research of Sichuan Intelligent Tolerance Design and Testing Engineering Research Center (Chengdu University of Information Technology) under Grant CCAT2023KF005, and in part by the Scientific Research of Neijiang Normal University under Grant 2023QN12.

ABSTRACT Surface topography filtering is a commonly used technique in various fields, and over the years, a variety of filters have been included in international standards. However, traditional filtering methods continue to suffer from significant fitting errors in the separation of surface topography (form, waviness and roughness). To address these issues, this study proposes a new filter algorithm based on an improved VMD method that incorporates some VME algorithm ideas. The proposed filter analyzes surface topography through three pivotal steps: Firstly, it derives the optimal robust weighting function. Secondly, it integrates the weighting function into the isotropic residual constraint VMD to decompose the surface into several isotropic modes (sub-surfaces). Ultimately, it quantitatively computes and combines the sub-surfaces to reconstruct the topography of each surface. Numerical simulation experiments illustrate that the proposed algorithm outperforms advanced surface filters, significantly reducing fitting errors of surface topography separation including areal-VMD-based filters. Finally, two grinding workpieces are analyzed using the proposed algorithm to demonstrate its effectiveness in evaluating machined surfaces, revealing the analytical process and presenting the results.

INDEX TERMS Surface filter, surface topography analysis, IRcVMD, VME.

NOMENCLATURE

VMD	variational mode decomposition.
EWT	empirical wavelet transform.
VME	variational mode decomposition.
EMD	empirical mode decomposition.
RrVMD	Residual-restrained variational mode decomposition.
IRcVMD	Isotropic Residual-constrained variational mode decomposition.
λ	The cut-off wavelength.
$U_k(x,y)$	The surface of the KTH iteration.
$m(x,y)$	The mode decomposed by VMD-based algorithm.
$r(x,y)$	Residual decomposed by VME-based algorithm.
H	Hilbert mask.
$\hat{\rho}_k(w_u, w_v)$	The frequency response of IRcVMD.
δ	The weight function.
PC	The person correlation coefficient.
RMSE	Root mean square error.

The associate editor coordinating the review of this manuscript and approving it for publication was Siddhartha Bhattacharyya.

I. INTRODUCTION

The performance of mechanical components is closely linked to their manufacturing process. These components can be analyzed using advanced surface analysis tools after surface machining, and a crucial step in the analysis is the precise and effective separation of surface topography features, such as form, waviness, and roughness. An effective method of accomplishing this is through filtering operations, which divide the surface into three wavelength ranges: low, medium, and high [1].

The mainstream Gaussian filter has been standardized in ISO GPS [2]; however, in certain practical industrial

applications it has some drawbacks such as shape distortion in the surface topography decomposed by it, sensitivity to outliers, and large fitting errors [3]. To overcome these issues, the M-estimation method can be used to improve this filtering method into a robust Gaussian filter, which effectively suppresses the problem of shape distortion [4]. A low-fitting error filtering method, which accurately reflects surface topography, is a popular research topic. For instance, spline filter [5] has been proposed to overcome the shortcomings of Gaussian filtering and is recommended by international standards. Its core principle is to solve the corresponding matrix through different boundary conditions to overcome the deformation problem. Its mathematical principles are similar to Butterworth filtering, and an algorithm for robust filter is listed in international standards [6]. Moreover, wavelet is another surface filtering method, which is better than the two filtering methods mentioned above in dealing with spectrum overlap. Its application in surface topography analysis greatly reduces the fitting error of roughness. It takes surface topography as input and directly outputs several sub-surfaces [7]. However, different wavelets have different filtering effects, which affect their generalization ability.

To minimize the fitting error during surface filtering, multi-resolution methods have been increasingly utilized in surface topography analysis. One example is a data-driven approach, which differs from wavelet-empirical mode decomposition(EMD) [8], that decomposes signals by solving their upper and lower envelopes, making it ideal for non-stationary signals. Despite some drawbacks, including modal aliasing and boundary effects, the EMD method has been extended and improved by experts [9], [10] to better reflect surface topography. Additionally, the empirical wavelet transform(EWT) [11] algorithm has proven successful by dividing the frequency domain into consecutive intervals and approximating orthogonal wavelets [12]. Applications of empirical wavelets in surface topography analysis have yielded positive results. However, accurately establishing the relationship with the cutoff wavelength remains a common issue in these methods. Furthermore, lack of robustness consideration and standardization in the industry also limits their effectiveness.

In the most recent version of ISO 25178-2 [13], linear profile parameters have been extended to two-dimensional (2D) areal surface parameters. In contrast to one-dimensional (1D) linear profiles, areal surface parameters are evaluated on an areal surface, which provides more information than one-dimensional linear profiles. Therefore, it is crucial to develop areal surface filtering. However, existing ISO international standards [2] only include standardized areal Gaussian filtering. When extending from one-dimensional filtering to areal filtering, it is essential to consider the isotropy problem. Some researchers have attempted to derive and design areal spline filtering. To overcome the isotropy problem, Tong et al. [14], [15] proposed high-order spline filtering by adding higher-order terms to analyze the worn bearing ball. New areal filtering methods are also applicable based on areal considerations. Li et al. [16] proposed a method based on extended areal-VMD to metrology the worn metal surfaces. However, the VMD-based method generated residual errors in form. To address this issue, Li et al. [17] proposed a residual-restrained VMD surface filter method to evaluate the grinding metal surface. However, decomposing the surface into modes using VMD-based method resulted in high computational complexity and energy loss. Shao et al. [18]. evaluate the discontinuous engineering surface topography using the discrete modal decomposition, and achieving favorable outcomes in the obtained results. He et al. [19]. uses improved complete ensemble empirical modal decomposition of adaptive noise to decompose the surface topography of the machined surface.

In light of the various factors leading to high fitting errors on surface topography separation discussed above, this study introduces a novel surface filtering method for the analysis of areal surfaces. Drawing inspiration from the principles of areal-VMD and variational mode extraction (VME) [20], as well as Butterworth bandpass filter [21], this new approach is called areal isotropic residual constrained VMD (IRcVMD) to applied on a grinding surface. Its primary innovation lies in achieving smaller fitting errors on surface topography separation compared to existing advanced filtering methods. The process of analyzing the surface topography using the robust IRcVMD method, which is presented in Fig.1.

The whole surface topography analysis process is divided into four parts, the part of parameter input corresponds to section three, it represents the areal IRcVMD's stage within the entire process of surface topography evaluation. The weight function calculation and acquisition of modes and residual, which is the implementation of robust IRcVMD, is put in sections IV, V-A, V-B, the part of surface topography parameter calculation corresponds to section V-C. Section two and section six are approach derivation and experiment respectively.

II. APPROACHES

In order to mitigate the spectral overlap between modes, the unoptimized modes and components can be regarded as residuals, including unrelated outliers. Unlike the traditional VMD algorithm, the aim here is to extract effective modes from these residuals through k times of optimization. Thus, based on this approach, under the areal condition, each surface $U_k(x,y)$ can be expressed as the sum of the current mode $m_k(x,y)$, residuals $r(x, y)$ and other modes, and its mathematical expression is given as follows:

$$U_k(x, y) = m_k(x, y) + r(x, y) + \sum_{i \neq k} m_i(x, y) \tag{1}$$

The equation for the updated mode optimization of areal-VMD is provided below [22]:

$$\hat{m}_k^{n+1}(w_u, w_v)$$

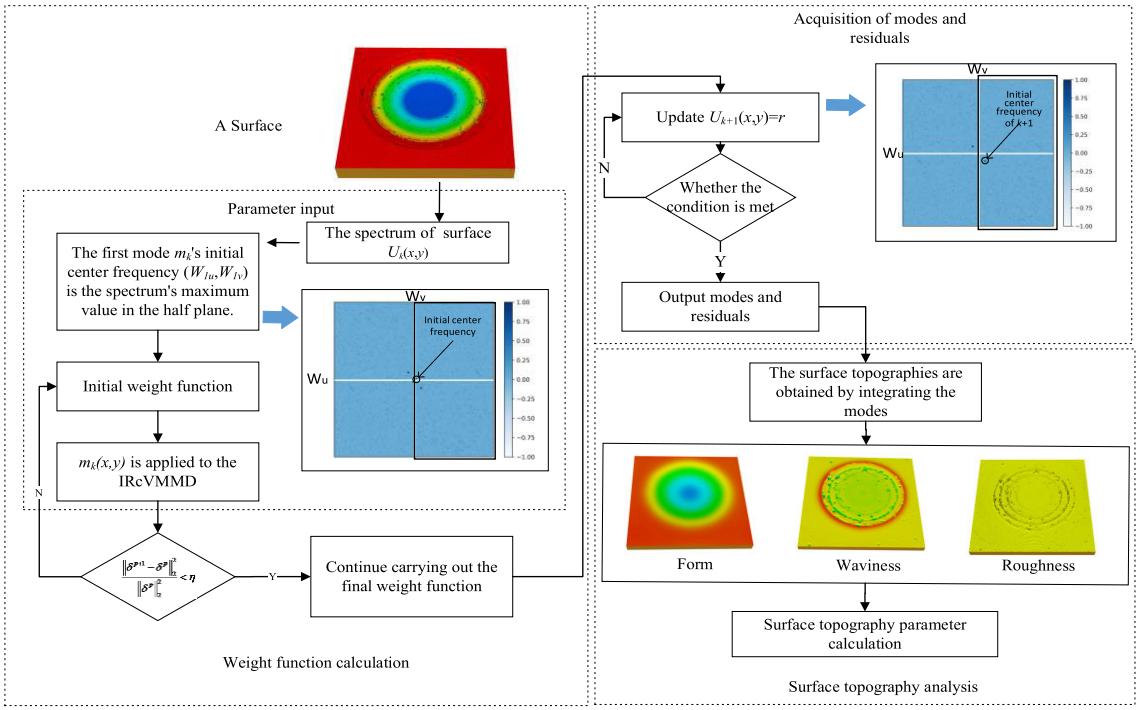

FIGURE 1. The algorithmic flowchart for surface topography analysis.

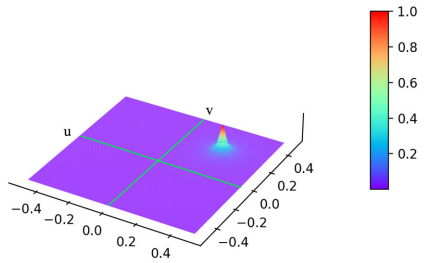

FIGURE 2. Amplitude-frequency characteristics of VMD-based filter.

$$H_k^{n+1}(w_u,w_v)(\hat{U}(w_u,w_v)-\sum_{i\neq k}\hat{m}_i^{n+1}(w_u,w_v)+\frac{\hat{\lambda}^n(w_u,w_v)}{2}) = \frac{}{1+\alpha[(w_u-w_{uk}^n)^2+(w_v-w_{vk}^n)^2]} \tag{2}$$

where H_k^{n+1} denotes the Hilbert Mask, $\hat{U}$ represents the input frequency domain signal, denotes the i-th mode, is a dual variable, represents a regularization parameter, and the amplitude-frequency characteristics of the areal-VMD filter are displayed in Fig.2. However, to achieve our research goal of making the separated residual and modal bandwidth more compact, a more appropriate modification is to reduce both the frequency response and residual of the current mode, as well as those of the other modes. Based on the analysis above, we can provide the frequency response of the mode in an isotropic state, which is expressed in the following equation:

$$\hat{\rho}_k(w_u,w_v)=\frac{w_u^2+w_v^2}{\alpha(w_u+w_v-\sqrt{w_{uk}^2+w_{vk}^2})^2} \tag{3}$$

where w_u and w_v represent the two frequency directions u and v in the frequency domain, respectively, and α is a penalty term that serves as the regularization parameter in areal-VMD. In the frequency domain, α is closely related to the filtering bandwidth, while w_{uk} and w_{vk} correspond to the center frequencies in the u and v directions, respectively. Fig.3 illustrates the amplitude-frequency characteristics of the modes within a specific frequency response range. Based on this, the optimization objectives and constraints of Isotropic Residual-Constrained VMD (areal IRcVMD) in the frequency domain can be equationted as shown in Eq.4 and Eq.5. In this equation, the residual and the convolution at the center frequency of other modes need to be infinitely amplified, ensuring that the resulting mode and residual exhibit high orthogonality. For comparison, the target optimization equation for RrVMD is presented as follows:

$$\min\left\{\begin{array}{l}\underbrace{\sum_k\left\|\nabla[m_{AS,k}(x,y)]e^{-j(xw_{uk}+yw_{vk})}\right\|_2^2}_{t_0}+\\ \underbrace{\left\|\rho_k(x,y)*[r(x,y)+\sum_{i\neq k}m_{AS,i}(x,y)]\right\|_2^2}_{t_1}+\\ \underbrace{\sum_{i\neq k}\left\|m_{AS,k}(x,y)*\rho_i(x,y)\right\|_2^2}_{t_2}\end{array}\right\} \tag{4}$$

$$s.t.\ U_k(x,y)=m_k(x,y)+r(x,y)+\sum_{i\neq k}m_i(x,y) \tag{5}$$

In this equation, t_1 is utilized to minimize the correlation between the current mode and residuals with the other modes; t_0 is analogous to the optimization of the original areal-VMD; t_2 is utilized to enhance the orthogonality between the current mode and the remaining modes. The equation for $m_{AS,k}$ is presented below:

$$\nabla[m_{AS,k}(x,y)] = \frac{\partial m_{AS,k}}{\partial x} + \frac{\partial m_{AS,k}}{\partial y} \tag{6}$$

According to the introduction of regularization parameters and the augmented Lagrangian method [22], [23], the problems presented in equations 4 and 5 can be restructured, and the objective can be reequationted as follows:

$$\min \left\{ \begin{array}{l} \alpha \sum\limits_k \left\| \nabla[m_{AS,k}(x,y)] e^{-j(xw_{uk}+yw_{vk})} \right\|_2^2 + \\ \left\| \rho_k(x,y) * [r_{AS}(x,y) + \sum\limits_{i\neq k} m_{AS,i}(x,y)] \right\|_2^2 + \\ \sum\limits_{i\neq k} \left\| m_{AS,k}(x,y) * \rho_i(x,y) \right\|_2^2 + \\ \frac{\tau}{2} \left\| U_k(x,y) - \sum\limits_{k=0} m_{AS,k}(x,y) - r_{AS}(x,y) \right\|_2^2 + \\ \left\langle \lambda(x,y), U_k(x,y) - \sum\limits_{k=0} m_{AS,k}(x,y) - r_{AS}(x,y) \right\rangle \end{array} \right\} \tag{7}$$

$$\Omega = \sqrt{(w_u - w_{uk})^2 + (w_v - w_{vk})^2} \tag{8}$$

In this equation, the step size is represented by τ, while the dual variable is denoted by λ. Equation 7 can be simplified and transformed into the following equation using Parseval's theorem [22]. To achieve the goal of the proposed IRcVMD, modifications are required on Ω in Equation 9. Specifically, the expression in Equation 8 is replaced with Equation 11. (9), as shown at the bottom of the next page, where $m_{AS,k}(x,y)$ and $r_{AS,k}(x,y)$ represent the areal analytical signals, which are obtained by simulating one-dimensional analytical signals in VMD. Their expanded expressions are presented in Equation 10. The calculation of Ω is transformed from Equation 8 to Equation 11, inspired by Butterworth bandpass filter [24], The transformation from Eq.8 to Eq.11 represents a difference of IRcVMD over VMD-based filter. This modification guarantees the amalgamation of sub-components with identical bandwidths in diverse directions into a singular mode, thereby obviating the necessity for an overly extensive decomposition of sub-components in varying directions into modes.

$$\begin{aligned} \hat{m}_{AS,k}(w_u, w_v) &= [1 + \mathrm{sgn}(ww_u + ww_v)]\hat{m}_k(w_u, w_v), \\ \hat{r}_{AS}(w_u, w_v) &= [1 + \mathrm{sgn}(ww_u + ww_v)]\hat{r}_k(w_u, w_v) \end{aligned} \tag{10}$$

$$\Omega = \frac{w_u + w_v - \sqrt{w_{uk}^2 + w_{vk}^2}}{\sqrt{w_u^2 + w_v^2}} \tag{11}$$

Based on the Alternating Directions Method of Multipliers (ADMM), the optimal solution can be derived from the half plane of the spectrum. Thus, for each mode $\hat{m}_k$, the following equation needs to be minimized in order to obtain its corresponding value:

$$\begin{aligned} &\hat{m}_k^{n+1}(w_u, w_v) \\ &= \min\{4\alpha \iint \Omega^2 \left|\hat{f}_k(w_u, w_v)\right|^2 dw_u dw_v \\ &\quad + \tau \iint \left| \hat{U}_k(w_u, w_v) - \sum_{k=0} \hat{m}_k(w_u, w_v) - \hat{r}(w_u, w_v) \right. \\ &\quad \left. + \frac{\hat{\lambda}(w_u, w_v)}{2} \right|^2 dw_u dw_v \\ &\quad + 2 \iint \left| \frac{w_u^2 + w_v^2}{\alpha(w_u + w_v - \sqrt{w_{uk}^2 + w_{vk}^2})^2} [\hat{r}(w_u, w_v) \right. \\ &\quad \left. + \sum_{i\neq k} \hat{m}_i(w_u, w_v)] \right|^2 dw_u dw_v\} \\ &\quad + 2 \sum_{i\neq k} \iint \left| \hat{m}_{AS,k}(w_u, w_v) \frac{w_u^2 + w_v^2}{\alpha(w_u + w_v - \sqrt{w_{uk}^2 + w_{vk}^2})^2} \right|^2 \\ &\quad \times dw_u dw_v \end{aligned} \tag{12}$$

In Equation 12, by solving the partial derivative of $\hat{m}_k$ and taking the solution where the extreme point is located, we can derive the following optimization equation for the mode:

$$\begin{aligned} &\hat{m}_k^{n+1}(w_u, w_v) \\ &= \frac{\hat{U}_k(w_u, w_v) - \sum\limits_{i\neq k} \hat{m}_i(w_u, w_v) - \hat{r}(w_u, w) + \frac{\hat{\lambda}(w_u, w_v)}{2}}{1 + 2\alpha \frac{(w_u + w_v - \sqrt{w_{uk}^2 + w_{vk}^2})^2}{w_u^2 + w_v^2} + \sum\limits_{i\neq k} \frac{(w_u^2 + w_v^2)^2}{\alpha^2 (w_u + w_v - \sqrt{w_{uk}^2 + w_{vk}^2})^4}} \end{aligned} \tag{13}$$

Obtain the residual r using the same method as mentioned above: (14), as shown at the bottom of the next page.

In practice, including the residuals in the mode optimization equation is unnecessary. Therefore, the equation for acquiring the residuals (equation 14) can be substituted into the mode optimization equation 13 to obtain the final mode optimization equation 15. It is noteworthy that the mode optimization is independent and not affected by other modes or residuals. This effectively eliminates the need to preset the parameter k(the number of modes) in the later stage. (15), as shown at the bottom of the next page.

Another crucial parameter that requires updating is the center frequency. The update equation is obtained by solving step-by-step as follows: (16), as shown at the bottom of the next page, where a represents various directions in the frequency domain. To achieve isotropic modes and prevent energy loss, the entire algorithm of IRcVMD can be summarized by Equations 17, 18, 19, and 20. Furthermore, it is evident that the amplitude-frequency characteristics (Fig.3) of the proposed algorithm have been altered when compared

to the VMD-based algorithm shown in Fig.2. (17)–(21), as shown at the bottom of the next page.

III. THE PARAMETERS OPTIMIZATION

The algorithm, which is based on VMD, falls under the category of multi-resolution methods, which differs significantly from low-pass filtering techniques such as spline filter [26] and Gaussian filter [6] when used for surface topography analysis. One prominent difference is that low-pass filtering can extract surface topography data via the cutoff wavelength, which serves a similar purpose as the penalty term a in the VMD-based algorithm. Consequently, optimizing a is necessary, indicating the need for dynamic changes of this parameter. As per Reference [27], the equation for calculating this parameter is given below:

$$\alpha_k = \frac{m_s^2}{4}\left(\frac{1}{1+e^{\log 10 \frac{2\sqrt{w_{ku}^2+w_{kv}^2}}{m_s}}} - 0.5\right)^2 \tag{22}$$

where u and v represent the two orientations of the spectrum, respectively; m_s denotes the sampling frequency, and w represents the angular frequency which is equivalent to multiplying the actual frequency by 2π.

The traditional VMD-based methods require pre-setting the number of modes k, which determines if the number of modes is reasonably decomposed and enhances the filtering effect. However, as mentioned earlier, in the algorithm proposed in this paper, the modes are independently optimized and do not rely on residues and other modes. Therefore, following ingenious design, this paper's algorithm reasonably avoids this point. Another aspect that needs optimizing in this algorithm, compared to the traditional areal-VMD algorithm, is the initial central frequency, primarily used to determine the mode's bandwidth and ensure reasonable decomposition. According to the reference report [18], the modes usually represent components with the primary energy in the signal. Accordingly, for this study's purposes, the initial central frequency of the modes to be obtained and optimized is determined as the frequency location where the amplitude is highest in the frequency domain. When mode optimization reaches the iteration threshold, the algorithm updates the original surface U to the residue r.

Therefore, when compared with traditional VMD-based methods, the advantages can be summarized as follows: 1) The parameter k is not pre-defined; 2) The inclusion of the residual term in Eq. 18 minimizes the spectral overlap between different modes, consequently mitigating the over-

$$\min\left\{\begin{array}{l}\alpha\sum\limits_k \left\|j\Omega\hat{m}_{AS,k}(w_u,w_v)\right\|_2^2 + \\ \left\|\hat{\rho}_k(w_u,w_v)[\hat{r}_{AS}(w_u,w_v)+\sum\limits_{i\neq k}\hat{m}_{AS,i}(w_u,w_v)]\right\|_2^2 + \\ \sum\limits_{i\neq k}\left\|\hat{m}_{AS,k}(w_u,w_v)\hat{\rho}_i(w_u,w_v)\right\|_2^2 + \\ \frac{\tau}{2}\left\|\hat{U}_k(w_u,w_v)-\sum\limits_{k=0}\hat{m}_{AS,k}(w_u,w_v)-\hat{r}_{AS}(w_u,w_v)+\frac{\hat{\lambda}(w_u,w_v)}{2}\right\|_2^2\end{array}\right\} \tag{9}$$

$$\hat{r}^{n+1}(w_u,w_v) = \frac{\frac{\alpha^2(w_u+w_v-\sqrt{w_{uk}^2+w_{vk}^2})^4}{(w_u^2+w_v^2)^2}(\hat{U}_k(w_u,w_v)-\sum\limits_{k=0}\hat{m}_k(w_u,w_v)+\frac{\hat{\lambda}(w_u,w_v)}{2})-\sum\limits_{i\neq k}\hat{m}_i(w_u,w_v)}{1+\frac{\alpha^2(w_u+w_v-\sqrt{w_{uk}^2+w_{vk}^2})^4}{(w_u^2+w_v^2)^2}} \tag{14}$$

$$\hat{m}_k^{n+1}(w_u,w_v) = \frac{\hat{U}_k(w_u,w_v)+\frac{\alpha^2(w_u+w_v-\sqrt{w_{uk}^2+w_{vk}^2})^4}{(w_u^2+w_v^2)^2}\hat{m}_k(w_u,w_v)+\frac{\hat{\lambda}(w_u,w_v)}{2}}{\left|1+2\alpha\frac{(w_u+w_v-\sqrt{w_{uk}^2+w_{vk}^2})^2}{w_u^2+w_v^2}+\sum\limits_{i\neq k}\frac{(w_u^2+w_v^2)^2}{\alpha^2(w_u+w_v-\sqrt{w_{uk}^2+w_{vk}^2})^4}\right|\left|1+\frac{\alpha^2(w_u+w_v-\sqrt{w_{uk}^2+w_{vk}^2})^4}{(w_u^2+w_v^2)^2}\right|} \tag{15}$$

$$w_a^{n+1}{}_k = \frac{\alpha\iint w_p\left|\hat{m}_k^{n+1}(w_u,w_v)\right|^2 dw_u dw_v - \frac{1}{\alpha^2}\iint\frac{\left|\hat{r}(w_u,w_v)+\sum\limits_{i\neq k}\hat{m}_i(w_u,w_v)\right|^2}{\frac{(w_u+w_v-\sqrt{w_{uk}^2+w_{vk}^2})^4}{(w_u^2+w_v^2)^2}(w_v-w_{pk}^n)}dw_u dw_v}{\alpha\iint\left|\hat{m}_k^{n+1}(w_u,w_v)\right|^2 dw_u dw_v}, \quad \forall a\in\{u,v\} \tag{16}$$

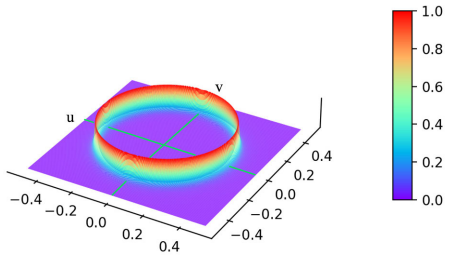

FIGURE 3. The approximate amplitude-frequency characteristics in IRcVMD.

lap between distinct surface topographies. 3)Unnecessary decomposition of modes is avoided, resulting in decreased energy loss and enhanced fitting accuracy of surface topography.

IV. ROBUST IRCVMD

A real engineering measurement surface often contains outliers and errors, and the presence of these values can significantly affect the benchmark(the sum of form and waviness) and eventually lead to inaccurate surface evaluation. While the IRcVMD algorithm discussed in this study theoretically segregates outliers and errors into high-frequency components, in reality, this is not the case, the necessity of robustness is illustrated in the experiment in section VI. Hence, to enhance the algorithm's robustness, we introduced the M-estimation method [28]. It is well-known that the robust weight function in the M-estimation theory requires optimization in the time domain. However, the algorithms proposed in this paper are optimized in the frequency domain. Since the Fourier transform is used in the time domain to frequency domain transformation, the mode optimization equation for robust IRcVMD is to do the Fourier transform for $\delta(x,y)U(x,y)$, where $\delta(x,y)$ is the robust weight function. Therefore, it is necessary to think about how to add a weight function to the equation 18. Finally the mode optimization *Equation 18* of IRcVMD is converted into the robust IRcVMD(Eq.23). (23), as shown at the bottom of the next page.

D is given by Equation 17. Having conducted numerous experiments and selected weight functions multiple times, the Andrews estimation method is ultimately chosen for use in this paper. Its calculation method is presented as follows:

$$\delta^i(x,y) = \begin{cases} \dfrac{1}{\pi v_i}\sin(\pi n_i) & |n_i| < 1 \\ 0 & |n_i| \geq 1 \end{cases}$$
$$n_i = U(x,y) - m_0^i(x,y) \Big/ \beta c \tag{24}$$

The expression of β is given as follows:

$$\beta = med\left|\frac{U(x,y) - m_0^i(x,y)}{std\left[U(x,y) - m_0^i(x,y)\right]}\right| \tag{25}$$

where c = 1.5π, which is a dynamically selected parameter. *std* represents the standard deviation, and *med* indicates that the median is required. Based on this, the complete process of the robust IRcVMD algorithm can be summarized using Algorithm 1.

V. THE CONNECTION BETWEEN MODE AND CUTOFF WAVELENGTHS

A. MODEL THE MODE AND CUT-OFF WAVELENGTH

In this study, wavelength should be used to ascertain the relationship between residual, mode, and surface topography categories. Therefore, surface U can be considered as a component in Equation 26, where a denotes form error, b represents waviness, and c represents roughness. Additionally, the relationship between the surface and the mode mentioned earlier allows the definition of the relationship between mode, surface topography, and the cut-off wavelength, which can be described by the model structure displayed in Fig.4. The

$$D = \frac{w_u + w_v - \sqrt{w_{uk}^2 + w_{vk}^2}}{\sqrt{w_u^2 + w_v^2}} \tag{17}$$

$$\hat{m}_k^{n+1}(w_u, w_v) = \frac{\hat{U}_k(w_u, w_v) - \sum_{i\neq k}\hat{m}_i(w_u, w_v) - \hat{r}(w_u, w_v) + \frac{\hat{\lambda}(w_u, w_v)}{2}}{1 + 2\alpha[D^2] + \sum_{i\neq k}\frac{1}{\alpha^2 D^4}} \tag{18}$$

$$\hat{r}^{n+1}(w_u, w_v) = \frac{\alpha^2 D^4(\hat{S}_k(w_u, w_v) - \sum_{k=0}\hat{m}_k(w_u, w_v) + \frac{\hat{\lambda}(w_u, w_v)}{2}) - \sum_{i\neq k}\hat{m}_i(w_u, w_v)}{1 + \alpha^2 D^4} \tag{19}$$

$$w_a^{n+1}{}_k = \frac{\iint w_p \left|\hat{m}_k^{n+1}(w_u, w_v)\right|^2 dw_u dw_v}{\iint \left|\hat{m}_k^{n+1}(w_u, w_v)\right|^2 dw_u dw_v}, \forall a \in \{u, v\} \tag{20}$$

$$\hat{\lambda}^{n+1}(w_u, w_v) = \hat{\lambda}^n(w_u, w_v) + \tau\left[\hat{U}(w_u, w_v) - \sum_{k=0}\hat{m}_k(w_u, w_v) - \hat{r}(w_u, w_v)\right] \tag{21}$$

Algorithm 1

Input a functional surface: $U_k(x, y)$

Initializing $(w_{1u}, w_{1v}) = frequencyofmax\{(w_{ku}, w_{kv})\}$, $\delta^0 \leftarrow \delta^p$, $\alpha_0 \leftarrow \alpha_k$

Repeat

$a \leftarrow \hat{u}a + 1$

$\delta^a = \begin{cases} \frac{1}{\pi t}\sin(\pi t_a) & |t_p| < 1 \\ 0 & |t_a| \geq 1 \end{cases}$

Repeat

$n \leftarrow n + 1$

Calculation Hilbert mask:

$H_k^{n+1}(w_u, w_v) \leftarrow 1 + sgn(w_u w_{ku}^n + w_v w_{kv}^n)$

Update $\hat{m}_k$ for all w_u, w_v:

$$\hat{m}_k^{n+1}(w_u, w_v) = \frac{\iint \delta(x,y)U(x,y)e^{-j2\pi(w_u x + w_v y)}dxdy - \sum_{i\neq k}\hat{m}_i(w_u,w_v) - \hat{r}(w_u,w_v) + \frac{\hat{\lambda}(w_u,w_v)}{2}}{1+2\alpha[D^2]+\sum_{i\neq k}\frac{1}{\alpha^2 D^4}}$$

$$\hat{r}^{n+1}(w_u, w_v) = \frac{\frac{\alpha^2(w_u+w_v-\sqrt{w_{uk}^2+w_{vk}^2})^4}{(w_u^2+w_v^2)^2}(\hat{U}_k(w_u,w_v) - \sum_{k=0}\hat{m}_k(w_u,w_v) + \frac{\hat{\lambda}(w_u,w_v)}{2}) - \sum_{i\neq k}\hat{m}_i(w_u,w_v)}{1+\frac{\alpha^2(w_u+w_v-\sqrt{w_{uk}^2+w_{vk}^2})^4}{(w_u^2+w_v^2)^2}}$$

Update w_{ku}, w_{kv}:

$$w_a^{n+1}{}_k = \frac{\iint w_p\left|\hat{m}_k^{n+1}(w_u,w_v)\right|^2 dw_u dw_v}{\iint\left|\hat{m}_k^{n+1}(w_u,w_v)\right|^2 dw_u dw_v}$$

$, \forall a \in \{u, v\}$

Dual Ascent:

$$\hat{\lambda}^{n+1}(w_u, w_v) = \hat{\lambda}^n(w_u, w_v) + \tau\left[\hat{U}(w_u, w_v) - \sum_{k=0}\hat{m}_k(w_u, w_v) - \hat{r}(w_u, w_v)\right]$$

Until convergence $\left\|\hat{m}_k^{n+1}(w_u, w_v) - \hat{m}_k^n(w_u, w_v)\right\|_2^2 < \varepsilon$

Until convergence

$\left\|\delta^{p+1} - \delta^p\right\|_2^2 < \eta$

Repeat

$k \leftarrow k + 1$

Repeat

$n \leftarrow n + 1$

$U_{k+1}(w_{ku}, w_{kv}) = \hat{r}^{n+1}(w_u, w_v)$

Update $\hat{m}_{k+1}$

Until convergence $\left\|\hat{m}_{k+1}^{n+1}(w_u, w_v) - \hat{m}_{k+1}^n(w_u, w_v)\right\|_2^2 < \varepsilon$

Until convergence $\left\|r^{n+1} - r^n\right\|_2^2 < \rho$

cut-off wavelength λ_f is utilized to differentiate form error from waviness, while the cut-off wavelength λ_c distinguishes waviness from roughness. The wavelength can be calculated using Equation 27, where f represents frequency.

$$U(x, y) = a(x, y) + b(x, y) + c(x, y) \tag{26}$$

$$\lambda = \frac{1}{f} \tag{27}$$

B. THE WAVELENGTH OF MODES

The method used to calculate modal frequency is the Riesz transform [29] because both the complete Hilbert transform and the partial Hilbert transform do not possess isotropic characteristics. Since the Riesz transform computes the instantaneous frequency in the original signal, the frequency features of the mode need to be integrated from instantaneous frequency data at all points.

$$\hat{m}_k^{n+1}(w_u, w_v) = \frac{\iint \delta(x, y)U(x, y)e^{-j2\pi(w_u x + w_v y)}dxdy - \sum_{i\neq k}\hat{m}_i(w_u, w_v) - \hat{r}(w_u, w_v) + \frac{\hat{\lambda}(w_u,w_v)}{2}}{1 + 2\alpha[D^2] + \sum_{i\neq k}\frac{1}{\alpha^2 D^4}} \tag{23}$$

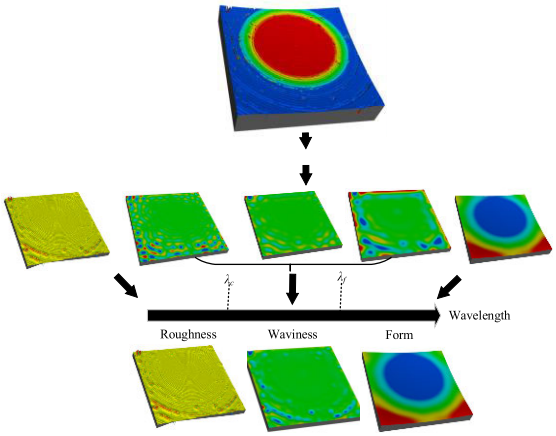

FIGURE 4. Relationship between modes, surface topography, and wavelength of cut-off wavelength.

TABLE 1. Common areal surface evaluation parameters and calculations.

Parameter	Calculation
S_q	$\sqrt{\frac{\iint h^2(x,y)dxdy}{A}}$
S_{sk}	$\frac{1}{S_q^3}\frac{\iint h^3(x,y)dxdy}{A}$
S_{ku}	$\frac{1}{S_q^4}\frac{\iint h^4(x,y)dxdy}{A}$

The calculation method of the Riesz transform in the frequency domain is shown below:

$$m_1(\Omega), m_2(\Omega) = \left\{-i\frac{w_u}{\|\Omega\|}\hat{m}(\Omega), -j\frac{w_v}{\|\Omega\|}\hat{m}(\Omega)\right\}, \quad \Omega = [w_u, w_v] \tag{28}$$

In the time domain, the monogenic signal obtained from the Riesz transform can be obtained through the inverse Fourier transform:

$$F_s(x,y) = \{m(x,y), im_1(x,y), jm_2(x,y)\} \tag{29}$$

For the phase, we can obtain it using the following Equation 30:

$$\varphi(x,y) = arctan\left(\frac{\|m_{1,2}(x,y)\|}{m(x,y)}\right) \tag{30}$$

Finally, the final instantaneous frequency can be obtained using Equation 31.

$$f_i = \sqrt{(\frac{\partial\varphi}{\partial x})^2 + (\frac{\partial\varphi}{\partial y})^2} \tag{31}$$

After the above steps, the surface topography within a certain cut-off wavelength range can be obtained, so as to complete the separation of surface topography.

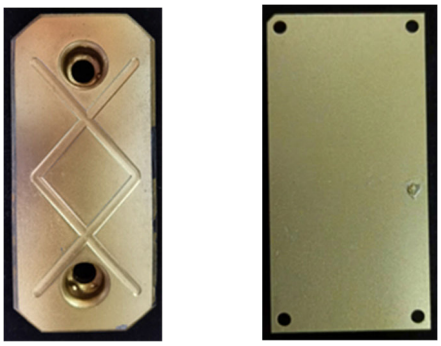

FIGURE 5. Two workpieces in the case.

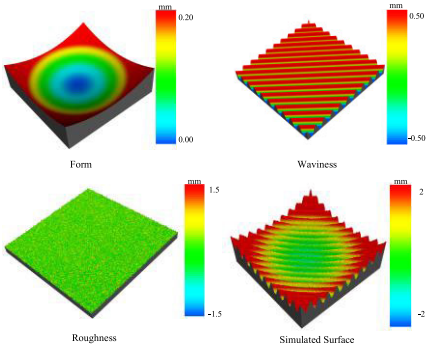

FIGURE 6. The simulated surface and surface topographies.

TABLE 2. The recommended cut-off wavelengths.

λ_f (mm)	λ_c (mm)	λ_f/λ_c
0.8	0.08	10
2.5	0.25	10
8	0.8	10

C. AREAL SURFACE PARAMETER CALCULATION

To obtain accurate information regarding a surface, it is imperative to analyze its areal surfaces. The ISO 25178 provides the definition of surface parameters for these surfaces. Assuming that the areal surface is denoted by h, the micro-surface topography parameters can be calculated using the method described in Table 1.

VI. EXPERIMENTS

A. EXPERIMENTAL CONDITIONS AND SIMULATION METHODS

In the experiment, two grinding metal workpiece surfaces are used to demonstrate the process of analyzing surface topography using the proposed robust areal IRcVMD algorithm. One is a workpiece with holes and grooves, while the other is a flat workpiece with holes. Their actual photos can be seen in Fig.5, with data acquisition being performed using a structured light photography system with an accuracy of 0.01mm. The performance of the algorithm is verified by applying it to a simulated surface expressed by an equation.

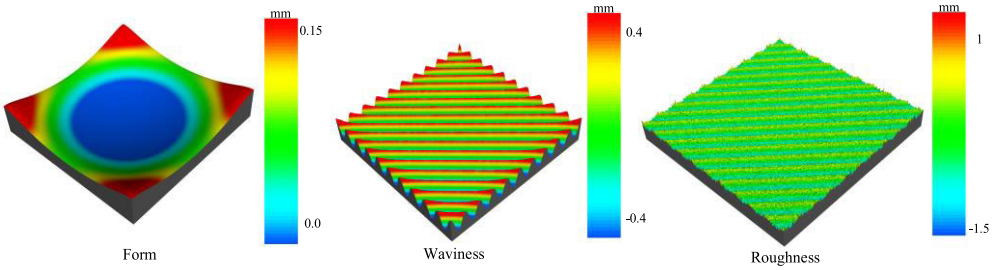

FIGURE 7. The surface topographies of areal Gaussian filter.

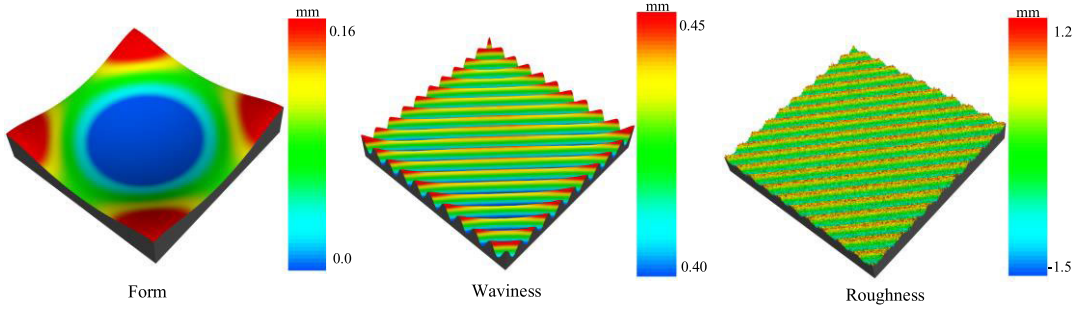

FIGURE 8. Surface topographies of spline filter.

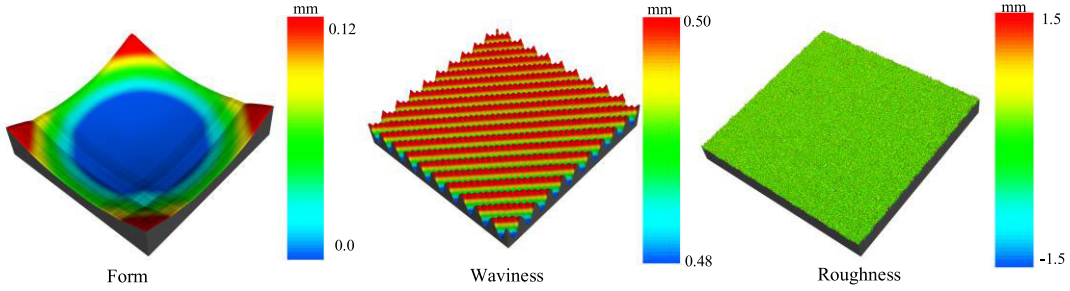

FIGURE 9. The surface topographies of wavelet.

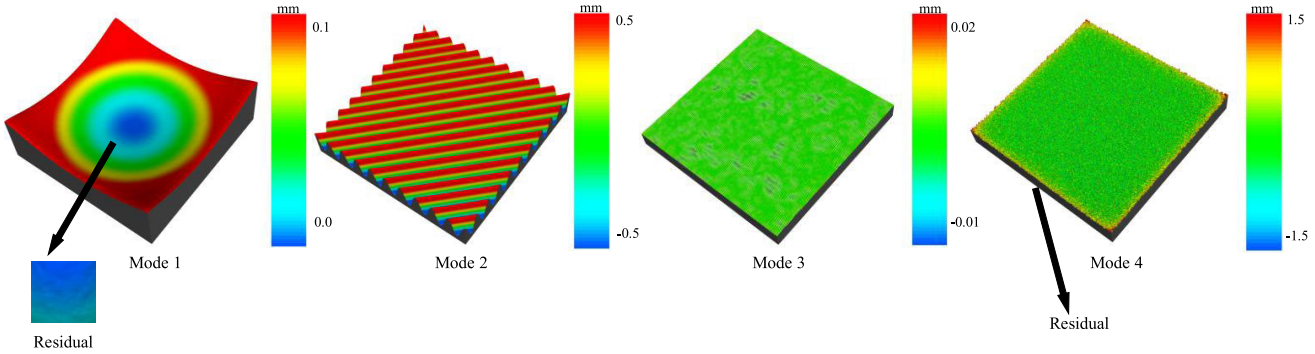

FIGURE 10. Modes by areal VMD.

In simulation experiments, the errors of different filtering separations indicating topography are verified, along with the deviation of the final calculated indicating topography parameter values, to reflect the performance of the filter. According to ISO 21920 [30], the algorithm is verified by utilizing the cut-off wavelength as shown in Table 2. The entire experiment is conducted using the Python programming environment.

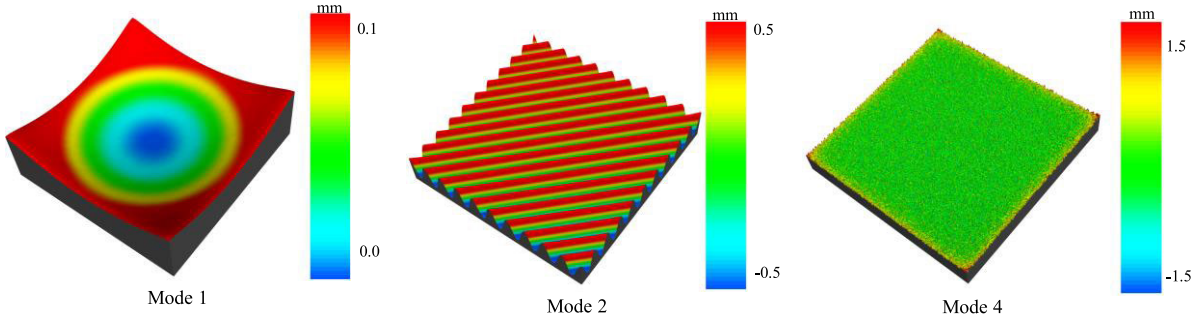

FIGURE 11. Surface topographies by areal VMD.

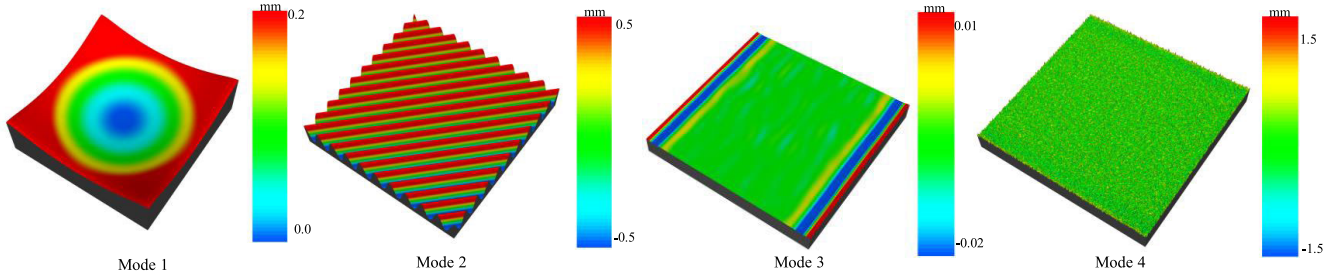

FIGURE 12. Modes by robust areal IRcVMD.

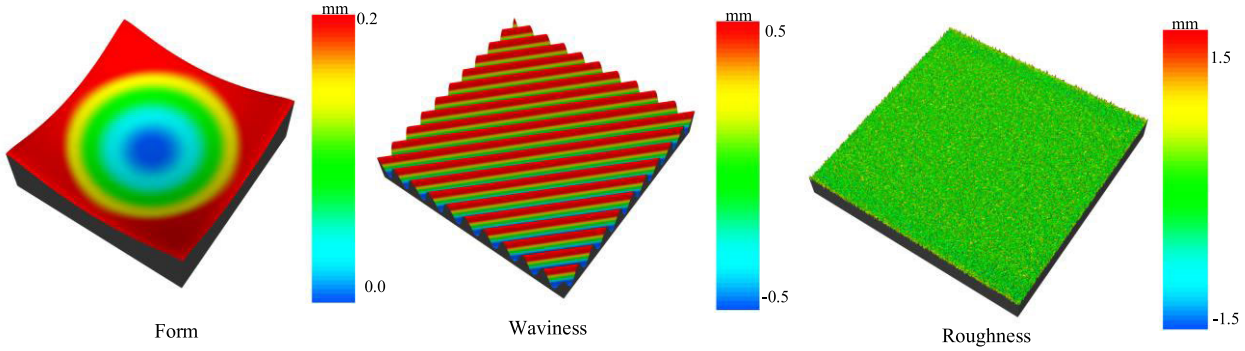

FIGURE 13. Surface topographies by robust areal IRcVMD.

B. NUMERICAL SIMULATION

Here, the benefits of the proposed areal IRcVMD algorithm are compared to those of other popular surface filters such as the areal Gaussian filter, the areal spline filter [25], the original areal VMD, and the wavelet filter. Numerical simulation is used to validate the fitting error of surface topography determined by these algorithms, as well as the extent of spectrum overlap. The expressions of filtering simulation surface are as follows:

$$0.1(x^2 + y^2) + 0.5\cos(10\pi x + 10\pi y) + 0.5normal(0, 0.8) \tag{32}$$

where the variables in Eq. 32 represent form, waviness, and roughness from left to right. Roughness is simulated using Gaussian noise, and the sampling size of the simulated surface is a square area with a side length of 2cm. The entire area contained 3600 points. The cut-off wavelengths are 2.5mm and 0.25mm, respectively, which are selected according to the recommendations of ISO 21920. To quantitatively evaluate the surface filtering performance, simulated surfaces and corresponding topographies are used, as shown in Fig.6. and Fig.7 illustrates the results of using an areal Gaussian filter with boundary expansion to eliminate boundary effects on the simulated surface. It is evident that the Gaussian filtering produces smooth results without any distortion in terms of form error. However, it can also be observed that there is some overlap between waviness and roughness. In contrast, Fig.9 displays the filtering outcomes of applying wavelet to the simulated surface, where the Daubechies wavelet is used to decompose the surface into six layers of wavelet coefficients. As can be seen, wavelet has an excellent filtering effect on

roughness, but its application leads to significant distortion in form error. This finding highlights the critical role of wavelet bases in separating surface topography.

Both the areal Gaussian filter and the areal spline filter are effective in form processing, but the areal spline filter produces superior results, as evidenced in Fig.8. However, this type of low-pass filtering also results in greater spectral overlap between intermediate and high frequencies, with only a 50% passing rate at the cut-off wavelength. The areal VMD algorithm is used to decompose the simulated surface into four modes, with a random initialization center frequency and a penalty parameter α of 4780. However, the surface topography decomposed by areal-VMD generated residuals in the form error, possibly due to the algorithm's lack of consideration for mode orthogonality. Despite the form error, the relevant modes, displayed in Fig.10, exhibit resilience in terms of waviness and roughness. As depicted in Fig.12, the proposed areal IRcVMD technique not only maintains the areal VMD's approximation ability for waviness and roughness but also eliminates residuals in the form error. Additionally, the filtering performance of areal IRcVMD surpasses that of other mainstream advanced filtering methods. Table 3 and Table 4 list the wavelengths of areal VMD and robust areal IRcVMD modes.

Subsequently, the Pearson correlation coefficient and root mean square error are used to quantitatively verify the similarity between the filtered surface topography and the simulated surface topography to make the verification results more accurate. The relevant equation is given as follows:

$$PC(a,b) = \frac{\sum_i \sum_j (a_{ij} - a)(b_{ij} - \widehat{b})}{\sqrt{\sum_i \sum_j (b_{ij} - \widehat{b})^2 \sum_i \sum_j (a_{ij} - a)^2}} \tag{33}$$

$$RMS(x,y) = \sqrt{\frac{\sum_{i=0}^{m} \sum_{j=0}^{n} (x_{ij} - y_{ij})^2}{mn}} \tag{34}$$

In this equation, a and b represent two different curved surfaces, while $\hat{a}$ and $\hat{b}$ denote their respective mean values. A lower RMSE value indicates smaller average differences, while a higher PC value indicates stronger correlations. Tables 6 and 7 provide PC and RMSE values for each algorithm. Table 5 shows the results of orthogonality tests carried out on surface topography adjacent to the cut-off wavelength based on the PC values. Compared with Gaussian filter and spline filter, the robus areal IRcVMD proposed in this paper performs better and can more accurately reflect surface texture information. Tables 10 and 11 show the differences between the simulated surface and the filtered surface after applying various filters.

C. THE SIMULATION OF ROBUSTNESS

The presence of an outlier significantly impacts the filtered surface topography, subsequently affecting the evaluation results. The subsequent experiment is centered around this issue as the research focus. A 50mm outlier is introduced at the center of the simulated surface. Fig.15 illustrates the form obtained through raw areal IRcVMD. Owing to the influence of the outlier, a bulge forms in the middle of the shape, as indicated by the arrow in the figure. However, after undergoing filtration using the areal robust IRcVMD, the bulge gradually diminishes with the algorithm's iteration, as demonstrated in Fig.16. Additionally, specific data is presented in Table 10, detailing the discrepancies between the filtered forms of raw areal IRcVMD, areal robust IRcVMD, and the baseline form. The experimental data demonstrate the algorithm's effectiveness in effectively mitigating the influence of outliers.

TABLE 3. The wavelength of modes in areal VMD calculated by Riesz transform.

Mode	Mode 0	Mode 1	Mode 2	Residual
Wavelength(mm)	24.35	0.709	0.203	0.116

TABLE 4. The wavelength of modes in robust areal IRcVMD calculated by Riesz transform.

Mode i	Mode 0	Mode 1	Mode 2	Residual
Wavelength(mm)	25.12	0.752	0.119	0.098

TABLE 5. The PC of each filter.

Filter	form -waviness	Waviness-roughness
Gaussian filter	15.67×10^{-3}	31.01×10^{-3}
Spline filter	15.88×10^{-3}	75.28×10^{-3}
DWT	9.404×10^{-3}	1.138×10^{-3}
Robust IRcVMD	0.381×10^{-3}	0.329×10^{-3}

TABLE 6. The PC of filters between filtered topography and baseline topography.

Filter	form	Waviness	roughness
areal Gaussian filter	0.9898	0.9874	0.9834
areal Spline filter	0.9903	0.9960	0.9911
areal DWT	0.9812	0.9849	0.9814
areal VMD	0.9809	0.9994	0.9904
areal Robust IRcVMD	0.9914	0.9999	0.9951

TABLE 7. The result of RMSE in different surface filter.

Filter	form	Waviness	roughness
areal Gaussian filter	6.312×10^{-3}	67.82×10^{-3}	56.42×10^{-3}
areal Spline filter	5.911×10^{-3}	42.68×10^{-3}	41.23×10^{-3}
areal DWT	12.48×10^{-3}	62.51×10^{-3}	51.76×10^{-3}
areal VMD	7.137×10^{-3}	9.121×10^{-3}	42.47×10^{-3}
areal Robust IRcVMD	6.100×10^{-3}	5.184×10^{-3}	30.78×10^{-3}

TABLE 8. The deviation D_i of the waviness parameters. the areal Gaussian filter-D1, areal DWT-D2, areal VMD-D3, robust areal IRcVMD-D4.

Parameter	Simulated	areal Gaussian filter	areal DWT	areal VMD	areal Robust IRcVMD	D1	D2	D3	D4
S_q	0.353	0.302	0.352	0.350	0.353	14.44%	0.28%	0.84%	0.00%
S_{sk}	7.191	6.001	6.901	7.699	7.578	16.54%	4.03%	7.06%	5.38%
S_{ku}	1.499	1.586	1.608	1.589	1.500	5.80%	6.77%	6.00%	0.06%

TABLE 9. The deviation D_i of the roughness parameters. the areal Gaussian filter-D1, areal DWT-D2, areal VMD-D3, robust areal IRcVMD-D4.

Parameter	Simulated	areal Gaussian filter	areal DWT	areal VMD	areal Robust IRcVMD	D1	D2	D3	D4
S_q	0.319	0.330	0.321	0.336	0.317	3.44%	0.62%	5.32%	0.62%
S_{sk}	0.016	0.019	0.018	0.017	0.017	12.50%	18.75%	6.25%	6.25%
S_{ku}	3.022	3.016	3.023	3.025	3.017	0.19%	0.03%	0.09%	0.16%

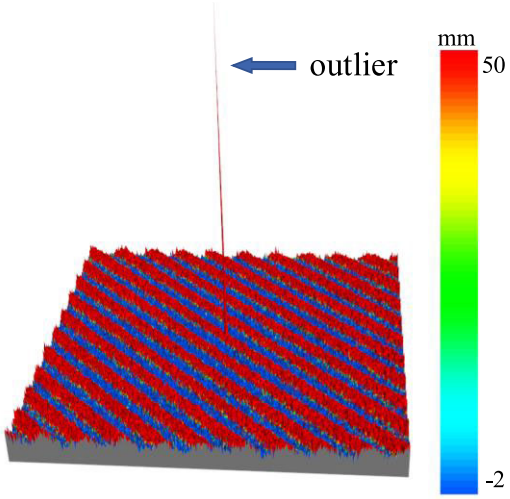

FIGURE 14. The simulated surface with outliers.

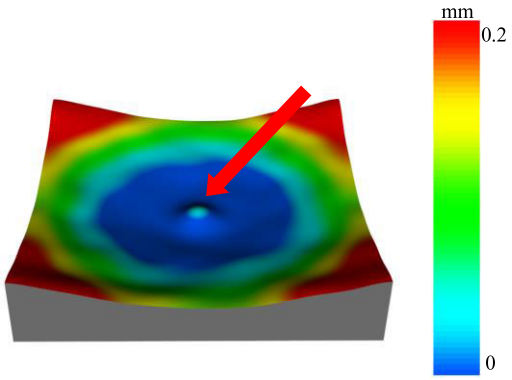

FIGURE 15. The form obtained by raw IRcVMD.

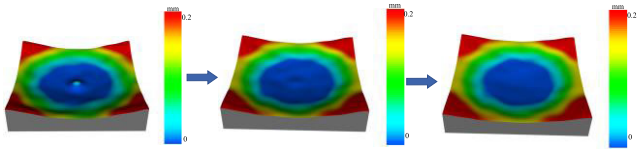

FIGURE 16. The form obtained after each iteration of the robust IRcVMD.

TABLE 10. The RMSE between filtered form and simulated form.

Index	IRcVMD	Robust IRcVMD
RMSE	1.341×10^{-2}	6.100×10^{-3}
PC	0.9128	0.9914

TABLE 11. Parameter of the area *a* in the metal flat workpiece.

Unit(*um*)	*Sq*	S_{sk}	S_{ku}
waviness	0.471	1.404	2.386
roughness	0.229	-0.032	3.252

TABLE 12. Parameter of area *b* in metal flat workpiece.

Unit(*um*)	*Sq*	S_{sk}	S_{ku}
waviness	0.296	0.724	2.315
roughness	0.209	-0.0606	3.216

TABLE 13. Parameters in the perforated workpiece.

Unit(*um*)	*Sq*	S_{sk}	S_{ku}
waviness	2.899	1.405	2.427
roughness	1.298	0.013	3.325

D. CASE STUDY

The case validates the filtering performance of various filtering algorithms on the surfaces of workpieces subjected to grinding by measuring the degree of spectrum overlap, the evaluation index employed is PC. Additionally, the case is

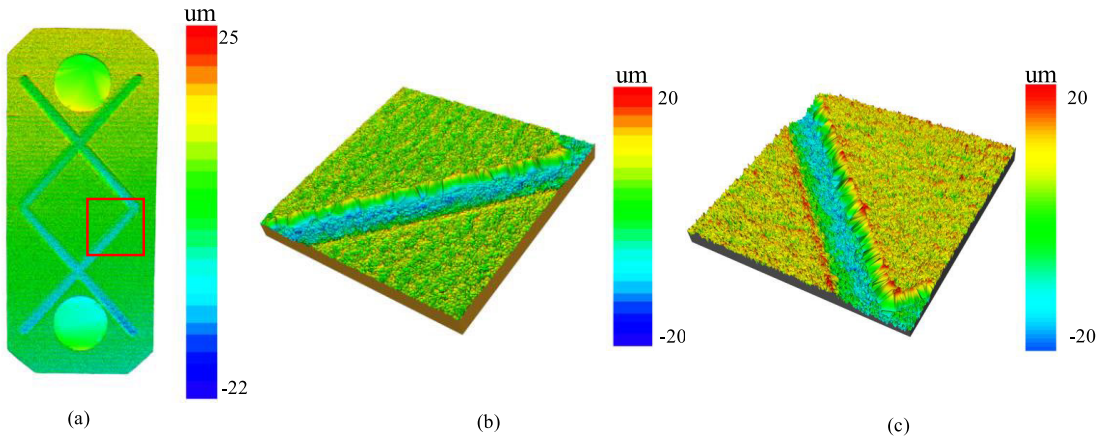

FIGURE 17. Perforated workpiece and its filtering area.

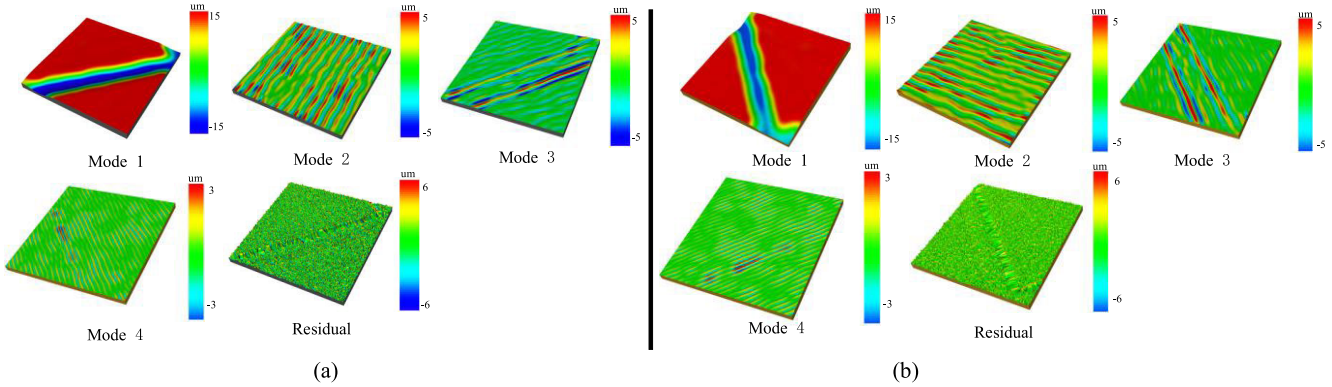

FIGURE 18. The result of robust areal IRcVMD for the same workpiece in two directions.

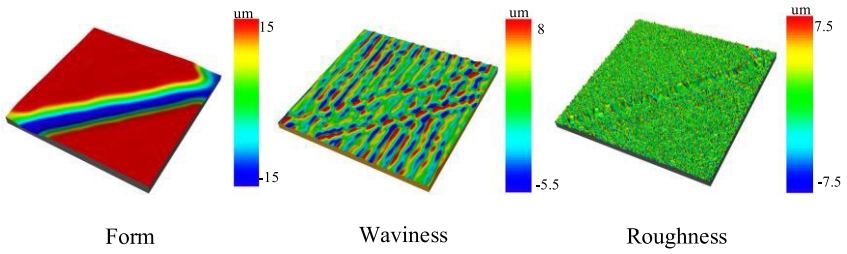

FIGURE 19. Surface topography reconstructed by robust areal IRcVMD.

also utilized to illustrate the algorithmic analysis process of surface topography.

1) THE PERFORATED WORKPIECE WITH RIDGES

The 78mm ×40mm metal workpiece with grooves depicted in Fig.13 is used for the first case study. The areal surface parameters described in Section IV are used to evaluate the surface of the red-boxed 8mm × 8mm area, with a sample interval of 0.01mm, the specification Ra =0.15μm. According to ISO 21920-3, λ_f is set to 8mm and λ_c is set to 0.5mm. To confirm that the application of the algorithm in various orientations does not impact the outcomes, the red region illustrated in Fig.17.b represents the positive direction, while Fig.17.c depicts the results following a 90° rotation. Subsequent to the algorithm execution, the surface modes for the positive direction and the 90° direction are presented in Fig.18.a and Fig.18.b respectively. Notably, it is observed that the modes are identical apart from the orientation; hence, the direction does not exert any influence on the results. As shown in Fig. 14, the signal is decomposed five times by using the proposed areal IRcVMD to obtain five modes and one residual. Fig.15 depicts the residual spectrum after extraction of each mode. In these modes, the first mode is

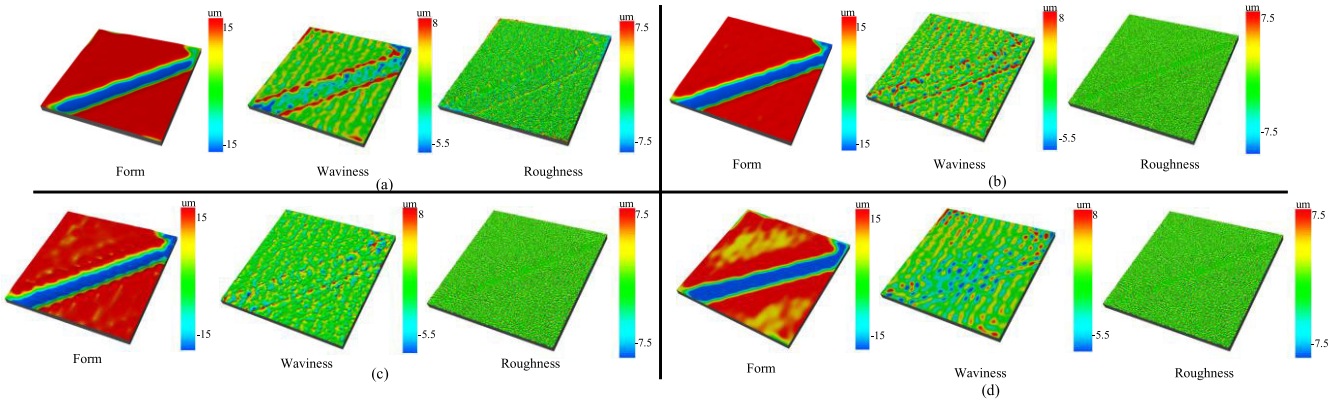

FIGURE 20. Surface topographies obtained by different filter. (a)The surface topographies obtained by areal gaussian filter; (b)The surface topographies obtained by areal spline filter; (c)The surface topographies obtained by areal VMD.

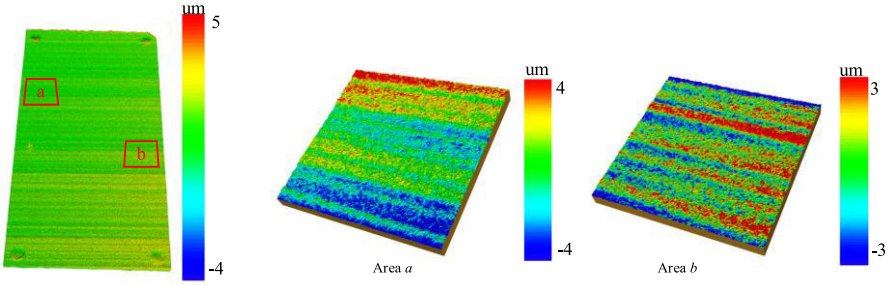

FIGURE 21. The metal flat workpiece with filtering area *a*, *b*.

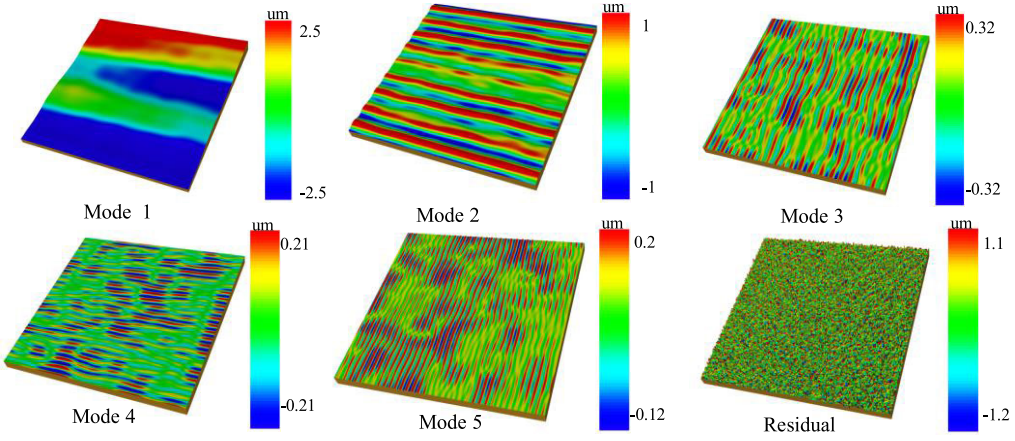

FIGURE 22. The result of robust areal IRcVMD.

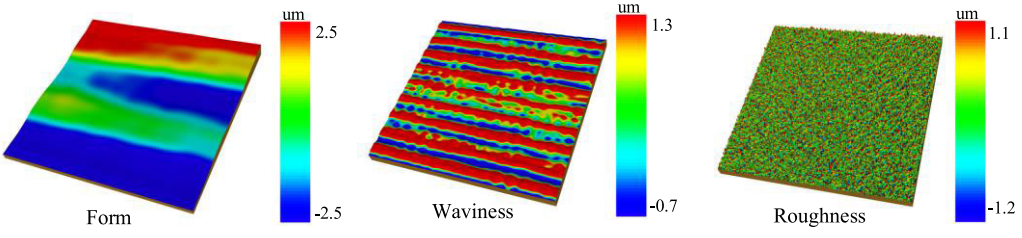

FIGURE 23. Surface topography reconstructed by robust areal IRcVMD.

characterized by form, the second through fifth modes by waviness, and the residuals by roughness with a tiny amount of form and waviness. As illustrated in Fig.16, the mode and wavelet are used to reconstruct surfaces in the matching cut-off wavelength range in order to get surface topographies. Table 13 summarizes three evaluation parameters.

The PC is used to measure the spectrum overlap of the surface topography obtained by different filter algorithms.

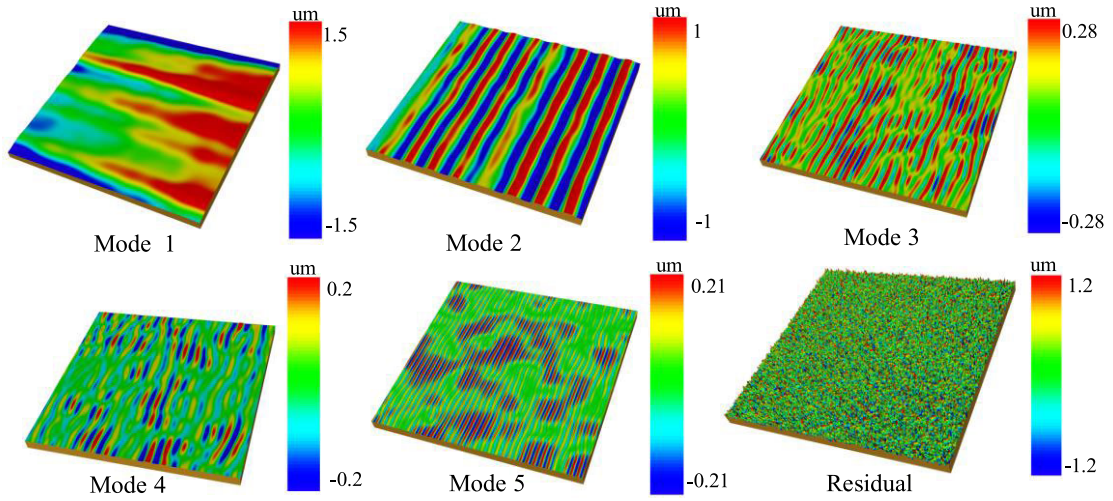

FIGURE 24. The result of area *b*.

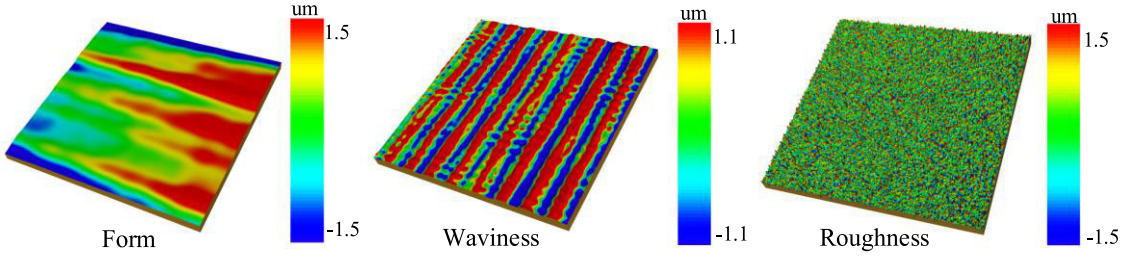

FIGURE 25. Surface topography reconstructed by robust areal IRcVMD.

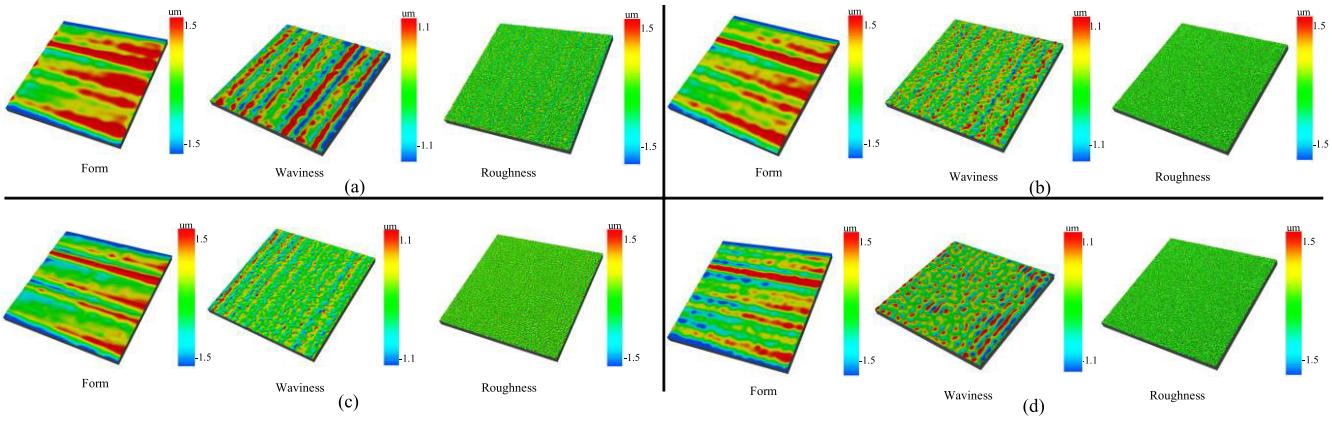

FIGURE 26. Surface topographies obtained by different filter. (a)The surface topographies obtained by areal gaussian filter; (b)The surface topographies obtained by areal spline filter; (c)The surface topographies obtained by areal VMD.

The surface topography obtained by the remaining four filters is shown in Fig.20, the PC values in Table 14 show that the proposed algorithm has the lowest spectrum overlap. This indicates that the proposed algorithm is suitable for grinding surfaces.

2) THE FLAT METAL WORKPIECE

As depicted in Fig.21, the second casing is a 60 mm × 30 mm metal plate. Two areas of 8mm × 8mm in the two red boxes (*a* and *b*) are selected to perform surface texture analysis, with a 0.01mm sample interval. The parameter $Ra = 0.1\mu$m allows for cutoff wavelengths of $\lambda_f = 2.5$mm and $\lambda_c = 0.25$mm. After filtered by the resilient areal IRcVMD, a total of five decompositions are performed to give five modes and one residual, as illustrated in Fig.22. It demonstrates that the modes are quite uniform and rarely intermixed with other modes. Roughness parameters and waviness parameters are depicted in Table 11. Area *b* is evaluated in the same manner,

TABLE 14. The PC between different surface topography by different filter methods in a perforated workpiece.

Filter	Areal Gaussian filter	Areal spline filter	Areal wavelet	Areal VMD	Areal Robust IRcVMD
Form-Waviness	0.435	0.426	0.422	0.432	0.045
Waviness-Roughness	0.242	0.309	0.028	0.300	0.021

TABLE 15. The PC between different surface topography by different filter methods in region *b* of a flat workpiece.

Filter	Areal Gaussian filter	Areal spline filter	Areal wavelet	Areal VMD	Areal Robust IRcVMD
Form-Waviness	0.493	0.400	0.175	0.345	0.054
Waviness-Roughness	0.200	0.293	0.072	0.219	0.065

and each mode is depicted in Fig.24; the surface topography is depicted in Fig.25, and the evaluation parameters are reported in Table 12.

The PC is used to measure the region *b* inside the flat workpiece as same, the filtering results and corresponding PC values are depicted in Fig.26 and Table 15, The findings indicate that the proposed algorithm exhibits a minimal degree of spectral overlap.

VII. CONCLUSION AND FUTURE WORK

In this paper, a new robust algorithm is proposed in the field of engineering surface filter. The classic two-dimensional VMD algorithm is extended and improved. The process of two-dimensional surface texture analysis based on robust areal IRcVMD is divided into four parts: weight function calculation, surface mode and residual decomposition, mode classification, and areal surface parameter calculation. The improved aspects can be found through experiment:

1) The simulation experiment demonstrates robust IRcVMD is superior to classical filter in PC and RMSE which reduces the fitting error of surface topography separation.
2) Through experimentation on grinding surface in the given case, it can be observed that the robust areal IRcVMD exhibits minimal spectral overlap, enabling superior separation of surface topography. This algorithm is well-suited for surfaces associated with this machining type.
3) The robust areal IRcVMD can suppress outlier effectively.

REFERENCES

[1] B. He, H. Zheng, S. Ding, R. Yang, and Z. Shi, "A review of digital filtering in evaluation of surface roughness," *Metrol. Meas. Syst.*, pp. 217–253, Feb. 2021.
[2] *Geometrical Product Specifications (GPS)-Filtration—Part 21: Linear Profile Filters: Gaussian Filters*, ISO Standard 16610-21, 2015.
[3] N. Cressie and D. M. Hawkins, "Robust estimation of the variogram: I," *J. Int. Assoc. Math. Geol.*, vol. 12, no. 2, pp. 115–125, Apr. 1980.
[4] H. Li, C. F. Cheung, X. Q. Jiang, W. B. Lee, and S. To, "A novel robust Gaussian filtering method for the characterization of surface generation in ultra-precision machining," *Precis. Eng.*, vol. 30, no. 4, pp. 421–430, Oct. 2006.
[5] H. Zhang, Y. Yuan, and W. Piao, "A universal spline filter for surface metrology," *Measurement*, vol. 43, no. 10, pp. 1575–1582, Dec. 2010.
[6] *Geometrical Product Specifications (GPS)-Filtration—Part 22: Linear Profile Filters: Spline Filters*, ISO Standard 16610-22, 2015.
[7] P. Bakucz and R. Krüger-Sehm, "A new wavelet filtering for analysis of fractal engineering surfaces," *Wear*, vol. 266, nos. 5–6, pp. 539–542, Mar. 2009.
[8] N. E. Huang, Z. Shen, S. R. Long, M. C. Wu, H. H. Snin, Q. Zheng, N. C. Yen, C. C. Tung, and H. H. Liu, "The empirical mode decomposition and the Hubert spectrum for nonlinear and non-stationary time series analysis," *Proc. Roy. Soc. A, Math., Phys. Eng. Sci.*, vol. 454, no. 1971, pp. 903–995, 1998.
[9] Z. Zhang, Y. Zhang, and Y. Zhu, "A new approach to analysis of surface topography," *Precis. Eng.*, vol. 34, no. 4, pp. 807–810, Oct. 2010.
[10] S. Du, T. Liu, D. Huang, and G. Li, "A fast and adaptive bi-dimensional empirical mode decomposition approach for filtering of workpiece surfaces using high definition metrology," *J. Manuf. Syst.*, vol. 46, pp. 247–263, Jan. 2018.
[11] J. Gilles, "Empirical wavelet transform," *IEEE Trans. Signal Process.*, vol. 61, no. 16, pp. 3999–4010, Aug. 2013.
[12] Y. Shao, S. Du, and H. Tang, "An extended bi-dimensional empirical wavelet transform based filtering approach for engineering surface separation using high definition metrology," *Measurement*, vol. 178, Jun. 2021, Art. no. 109259.
[13] *Geometrical Product Specifications (GPS)-Surface Texture: Areal—Part 2: Terms, Definitions and Surface Texture Parameters*, ISO Standard 25178-2, 2021.
[14] H. Zhang, M. Tong, and W. Chu, "An areal isotropic spline filter for surface metrology," *J. Res. Nat. Inst. Standards Technol.*, vol. 120, p. 64, Mar. 2015.
[15] S. Huang, M. Tong, W. Huang, and X. Zhao, "An isotropic areal filter based on high-order thin-plate spline for surface metrology," *IEEE Access*, vol. 7, pp. 116809–116822, 2019.
[16] Z. Li, Y. Xu, T. Li, Y. Shi, X. Jiang, Y. Cao, W. Zeng, Z. Xu, C. Zhang, and J. Huang, "Bi-dimensional variational mode decomposition for surface texture analysis," *Proc. CIRP*, vol. 114, pp. 36–41, Jan. 2022.
[17] Z. Li, Y. Xu, C. Zhang, C. Kong, I. Macleod, T. Li, X. Jiang, B. Guo, and J. Lu, "A robust areal residual-restrained variational mode decomposition for filtering on surface texture analysis," *Surf. Topography, Metrol. Properties*, vol. 11, no. 1, Mar. 2023, Art. no. 014005.
[18] Y. Shao, F. Xu, J. Chen, J. Lu, and S. Du, "Engineering surface topography analysis using an extended discrete modal decomposition," *J. Manuf. Processes*, vol. 90, pp. 367–390, Mar. 2023.
[19] G. He, H. Wang, Y. Sang, and Y. Lv, "An improved decomposition algorithm of surface topography of machining," *Machining Sci. Technol.*, vol. 24, no. 5, pp. 781–809, Sep. 2020.
[20] M. Nazari and S. M. Sakhaei, "Variational mode extraction: A new efficient method to derive respiratory signals from ECG," *IEEE J. Biomed. Health Informat.*, vol. 22, no. 4, pp. 1059–1067, Jul. 2018.
[21] D. Govind, B. Ginley, B. Lutnick, J. E. Tomaszewski, and P. Sarder, "Glomerular detection and segmentation from multimodal microscopy images using a Butterworth band-pass filter," Dept. Int. Soc. Opt. Photon., Université de Grenoble, Grenoble, France, Tech. Rep. 10581, 2018.
[22] K. Dragomiretskiy and D. Zosso, "Two-dimensional variational mode decomposition," in *Energy Minimization Methods in Computer Vision and Pattern Recognition* (Lecture Notes in Computer Science, Including Subseries Lecture Notes in Artificial Intelligence and Lecture Notes in Bioinformatics). Cham, Switzerland: Springer, 2015.
[23] M. Nazari and S. M. Sakhaei, "Successive variational mode decomposition," *Signal Process.*, vol. 174, Sep. 2020, Art. no. 107610.

[24] S. F. Hussin, G. Birasamy, and Z. Hamid, "Design of Butterworth bandpass filter," *Politeknik Kolej Komuniti J. Eng. Technol.*, vol. 1, no. 1, pp. 32–46, Dec. 2016.
[25] D. Janecki, "A two-dimensional isotropic spline filter," *Precis. Eng.*, vol. 37, no. 4, pp. 948–965, Oct. 2013.
[26] *Geometrical Product Specification (GPS)-Filtration—Part 61: Linear Areal Filters-Gaussian Filters*, ISO Standard 16610-61, 2015.
[27] J. Li, X. Yao, H. Wang, and J. Zhang, "Periodic impulses extraction based on improved adaptive VMD and sparse code shrinkage denoising and its application in rotating machinery fault diagnosis," *Mech. Syst. Signal Process.*, vol. 126, pp. 568–589, Jul. 2019.
[28] H. Zhang, J. Zhang, J. Hua, and Y. Z. Cheng, "A robust spline filter algorithm based on M-estimate theory," *Adv. Mater. Res.*, vols. 655–657, pp. 909–912, Jan. 2013.
[29] M. Felsberg and G. Sommer, "The monogenic signal," *IEEE Trans. Signal Process.*, vol. 49, no. 12, pp. 3136–3144, Dec. 2001.
[30] *Geometrical Product Specification (GPS)-Surface Texture: Profile—Part 2: Terms, Definitions and Surface Texture Parameters*, ISO Standard 21920-2, 2021.

QIN WEN received the master's degree from the School of Software Engineering, Chengdu University of Information Technology. She is currently a Teacher with Neijiang Normal University, Sichuan, China. Her current research interests include meteorological big data and precise measurement of instruments and meters.

NIANQING TANG is currently a Professor with the School of Artificial Intelligence, Neijiang Normal University. He is also a researcher in the fields of computer application and optimal control. Previously, he was the Deputy Dean of teaching with the School of Computer Science. He holds the position of the Secretary with the Artificial Intelligence School, Neijiang Normal University.